Assessing Photoreceptor Structure in Retinitis Pigmentosa and Usher Syndrome

Lynn W. Sun,[1] Ryan D. Johnson,[1] Christopher S. Langlo,[2] Robert F. Cooper,[3] Moataz M. Razeen,[1,4] Madia C. Russillo,[1] Alfredo Dubra,[1–3,5] Thomas B. Connor Jr,[1] Dennis P. Han,[1] Mark E. Pennesi,[6] Christine N. Kay,[7] David V. Weinberg,[1] Kimberly E. Stepien,[1] and Joseph Carroll[1–3,5]

[1]Department of Ophthalmology, Medical College of Wisconsin, Milwaukee, Wisconsin, United States
[2]Department of Cell Biology, Neurobiology & Anatomy, Medical College of Wisconsin, Milwaukee, Wisconsin, United States
[3]Department of Biomedical Engineering, Marquette University, Milwaukee, Wisconsin, United States
[4]Alexandria Faculty of Medicine, Alexandria University, Alexandria, Egypt
[5]Department of Biophysics, Medical College of Wisconsin, Milwaukee, Wisconsin, United States
[6]Casey Eye Institute, Oregon Health & Science University, Portland, Oregon, United States
[7]Vitreo Retinal Associates, Gainesville, Florida, United States

Correspondence: Joseph Carroll, Eye Institute, Room 830, 925 North 87th Street, Milwaukee, WI 53226, USA; jcarroll@mcw.edu.

Submitted: September 22, 2015
Accepted: March 4, 2016

Citation: Sun LW, Johnson RD, Langlo CS, et al. Assessing photoreceptor structure in retinitis pigmentosa and Usher syndrome. *Invest Ophthalmol Vis Sci*. 2016;57:2428–2442. DOI:10.1167/iovs.15-18246

Purpose. The purpose of this study was to examine cone photoreceptor structure in retinitis pigmentosa (RP) and Usher syndrome using confocal and nonconfocal split-detector adaptive optics scanning light ophthalmoscopy (AOSLO).

Methods. Nineteen subjects (11 RP, 8 Usher syndrome) underwent ophthalmic and genetic testing, spectral-domain optical coherence tomography (SD-OCT), and AOSLO imaging. Split-detector images obtained in 11 subjects (7 RP, 4 Usher syndrome) were used to assess remnant cone structure in areas of altered cone reflectivity on confocal AOSLO.

Results. Despite normal interdigitation zone and ellipsoid zone appearance on OCT, foveal and parafoveal cone densities derived from confocal AOSLO images were significantly lower in Usher syndrome compared with RP. This was due in large part to an increased prevalence of non-waveguiding cones in the Usher syndrome retina. Although significantly correlated to best-corrected visual acuity and foveal sensitivity, cone density can decrease by nearly 38% before visual acuity becomes abnormal. Aberrantly waveguiding cones were noted within the transition zone of all eyes and corresponded to intact inner segment structures. These remnant cones decreased in density and increased in diameter across the transition zone and disappeared with external limiting membrane collapse.

Conclusions. Foveal cone density can be decreased in RP and Usher syndrome before visible changes on OCT or a decline in visual function. Thus, AOSLO imaging may allow more sensitive monitoring of disease than current methods. However, confocal AOSLO is limited by dependence on cone waveguiding, whereas split-detector AOSLO offers unambiguous and quantifiable visualization of remnant cone inner segment structure. Confocal and split-detector thus offer complementary insights into retinal pathology.

Keywords: retinitis pigmentosa, Usher syndrome, adaptive optics, AOSLO, split-detector

Retinitis pigmentosa (RP) refers to a diverse group of inherited retinal degenerative disorders with a combined prevalence of approximately 1 in 4000. Functionally, RP is characterized by impaired night vision, slowly progressive peripheral-to-central visual field loss, and, often, an eventual decline in visual acuity. Fundus features including retinal pigment epithelium (RPE) changes, blood vessel attenuation, cystoid macular edema, disc pallor, and peripheral bone-spicule development are seen in various stages of RP. In addition, there is a prominent transition zone (TZ) from relatively healthy central retina to more severely affected peripheral retina, which can now be directly visualized using optical coherence tomography (OCT).[1] Of particular interest is the apparent correlation between measures of visual function and the integrity of the hyperreflective photoreceptor bands seen on OCT.[2–12] Although this approach provides a general framework for assessing the structure–function relationship in RP, the limited lateral resolution of current OCT precludes direct cellular level examination of rod and cone structure. Undetectable subtle changes in photoreceptor structure may explain observed dissociations between visual function metrics and OCT findings in a number of retinal diseases.[4,13] In contrast, adaptive optics (AO) ophthalmoscopes enable noninvasive visualization of the photoreceptor mosaic with cellular resolution.[14–16] It has been shown in a number of retinal conditions that significant photoreceptor disruption can be seen with AO imagery even when photoreceptor bands appear intact on OCT.[17–22] Numerous groups have examined the cone mosaic in RP using flood-illuminated AO[23,24] and confocal AO scanning light ophthalmoscopy (AOSLO).[25–31] In the presence of normal outer retinal architecture on OCT, foveal/parafoveal cone density in RP subjects can range from normal to severely decreased.[25,27,28,30,31] Furthermore, visual function can remain within normal limits even when the cone mosaic is disrupt-

ed.[21,27] These findings further highlight the superior sensitivity of AO imaging tools for assessing rod and cone mosaic structure in RP.

However, visualization of photoreceptors on both flood-illuminated AO and confocal AOSLO is thought to rely on propagation and reflectance of an electromagnetic wave along the longitudinal axis of the photoreceptor (i.e., waveguiding), which depends on intact photoreceptor structure.[32,33] In retinal degenerations, photoreceptors undergo morphologic changes[34–37] that disrupt normal waveguiding[38]; as a result, cones can have significantly altered reflective properties.[18,20,25,33,39–41] Moreover, cone reflectivity fluctuates over time,[42–46] and it has even been shown that cones with diminished reflectivity from a variety of retinal insults can spontaneously recover normal reflectivity.[20,33,47] As such, the reliance on normal waveguiding for cone visualization presents an inherent confound in analyzing and interpreting confocal AOSLO or AO flood illumination images of the cone mosaic: decreased cone density could be due to altered cone reflectivity or true loss of cone cells.

Recently it has been shown that nonconfocal split-detector AOSLO (henceforth referred to as "split-detector") can resolve cone inner segments independent of whether a cone has normal reflectivity on confocal AOSLO.[32] The ability to decouple cone visualization from their waveguide properties allows accurate assessment of remnant cone structure in retinal degenerations such as RP. Such measures may be important for identifying subjects most likely to benefit from emerging gene therapy treatments,[48] as well as monitoring the therapeutic effect of any intervention.[26] Of particular interest is the TZ in subjects with RP (including Usher syndrome). It has been posited that the TZ might represent a valuable model for understanding the longitudinal changes taking place at a given retinal location, providing insight into the natural history of the disease without necessarily examining the same retina over time.[6] Here we sought to examine cone structure across the TZ in a group of subjects with RP using both confocal and split-detector AOSLO and correlated these findings to the appearance of the photoreceptor bands on OCT. This multimodal imaging approach provides a more complete picture of photoreceptor structure and may be useful in evaluating cone structure in other conditions with TZs, such as choroideremia and Stargardt disease.

Methods

Subjects and Clinical Phenotyping

Research procedures followed the tenets of the Declaration of Helsinki. Informed written consent was obtained from all subjects after explanation of the nature and possible consequences of the study. The study protocol was approved by the institutional review board of the Medical College of Wisconsin. Subjects with clinically diagnosed RP and allied disorders were eligible for inclusion. After exclusion of subjects with inferior image quality due to corneal defects, media opacity, retinal edema, high refractive errors (greater than ±10 diopters [D]), 19 subjects were included in the study (11 with RP, 8 with Usher syndrome). One subject with autosomal recessive RP (ARRP) had unilateral disease (TC_0664). Two subjects with Usher syndrome were siblings (KS_1077 and JC_1088). Sixteen healthy subjects (11 male, 5 female; mean ± SD age = 27.3 ± 19.9 years; normal fundus appearance and no known ocular disease) were recruited as controls for the cone diameter measurements.

Best-corrected visual acuity (BCVA) was assessed in all subjects using a standardized Early Treatment of Diabetic Retinopathy Study (ETDRS) chart. Visual field was determined with an automated 10-2 Humphrey Visual Field Assessment (HVF; Carl Zeiss Meditec, Dublin, CA, USA). Axial length was measured using a Zeiss IOL Master (Carl Zeiss Meditec) to determine the micrometers per degree scale for each subject. Prior to all retinal imaging, the eye to be imaged was dilated and cyclopleged through topical application of phenylephrine hydrochloride (2.5%; Bausch & Lomb, Inc., Tampa, FL, USA) and tropicamide (1%; Akorn, Inc., Lake Forest, IL, USA). Fundus color photographs were taken in all subjects using a Zeiss VisuCam 200NM (Carl Zeiss Meditec) and/or an OPTOS Ultra-Widefield fundus camera (Optos plc, Dunfermline, Scotland, United Kingdom).

Genetic Testing and Predictions

Whole blood samples were collected from 18 of 19 subjects and screened for known autosomal dominant RP (ADRP), ARRP, X-linked RP (XLRP), and Usher syndrome mutations. JC_1157 had independently sought genetic testing by Asper Laboratories (Asper Biotech, Tartu, Estonia), and the subject provided results at the time of imaging; thus, a new sample was not collected. Genetic testing for IE_0508 was performed at the John and Marcia Carver Nonprofit Genetic Testing Laboratory (University of Iowa, Ames, IA, USA); for KS_0588, at the National Ophthalmic Disease Genotyping and Phenotyping Network (eyeGENE, National Eye Institute, Bethesda, MD, USA); and for JC_1183, at Prevention Genetics (Prevention Genetics, Marshfield, WI, USA). Molecular genetic analysis for the 15 remaining subjects was performed at the Casey Eye Institute Molecular Diagnostics Laboratory (Oregon Health & Science University, Portland, OR, USA).

Amino acid changes due to gene mutations were determined using Mutation Taster, which is available in the public domain at http://www.mutationtaster.org. Likely pathogenicity of previously unreported mutations resulting in amino acid changes was determined using Sorting Intolerant From Tolerant (SIFT), Protein Variation Effect Analyzer (PROVEAN), and PolyPhen-2 analysis tools. SIFT 1.03 and PROVEAN 1.1.3 are available in the public domain at http://provean.jcvi.org/index.php. SIFT reports likely tolerability of mutations; results are considered tolerated if the tolerance index is >0.05 and damaging if the tolerance index is ≤ 0.05. PROVEAN reports results as neutral or deleterious based on averaged δ alignment scores. Scores less than -2.5 were considered deleterious. PolyPhen-2 2.2.2 is available in the public domain at http://genetics.bwh.harvard.edu/pph2. PolyPhen-2 appraises mutations as benign, possibly damaging, or probably damaging based on the model's false-positive rate. PolyPhen-2 scores range between 0 (most probably benign) and 1 (most probably damaging). Cutoffs were 0.90 for possibly damaging and 0.95 for probably damaging.

Spectral-Domain Optical Coherence Tomography

Volumetric images of the macula were obtained in both eyes in all subjects (Cirrus HD-OCT; Carl Zeiss Meditec). Volumes were nominally 6×6 mm and consisted of 128 B-scans (512 A-scans per B-scan). Retinal thickness was calculated automatically using the built-in macular analysis software (v. 5.0), which measures the difference between the inner limiting membrane (ILM) and RPE boundaries.

Additional high-resolution scans were acquired in all subjects (Bioptigen SD-OCT; Bioptigen, Research Triangle Park, NC, USA). High-density line scans (nominal scan length, 7 mm, 1000 A-scans per B-scan, 100 repeated B-scans) were acquired both horizontally and vertically through the foveal center. Line scans were registered and averaged to reduce speckle noise in

Investigative Ophthalmology & Visual Science

the image as previously described.[49] Volumetric scans, nominally 7 × 7 mm in size, consisted of 250 B-scans (700 A-scans per B-scan), with two volumes acquired for each subject (horizontal and vertical orientation). En face scans were generated from the horizontal volumes using previously described custom segmentation software.[50]

Analysis of Photoreceptor Bands on Spectral-Domain Optical Coherence Tomography Images

Longitudinal reflectivity profiles (LRPs) from the SD-OCT line scans were generated as previously described.[22,51,52] Four layers were manually identified in resultant LRPs (external limiting membrane, ELM; ellipsoid zone, EZ; interdigitation zone, IZ; and the RPE/Bruch's membrane complex, RPE). Retinal areas where all four layers were visible as distinct peaks on the LRP were considered pre-TZ (normal) areas. The point at which the IZ peak disappeared was considered the beginning of the TZ, with the point at which the EZ peak disappeared considered the end of the TZ. Finally, the point at which the ELM peak merges with the RPE peak was considered the point at which the ELM and overlying inner retinal anatomy has collapsed onto the basement epithelium of the retina. The total width of the TZ, from nasal to temporal terminations and from superior to inferior terminations, was measured in all 19 subjects using the SD-OCT scans obtained horizontally and vertically through the fovea (for a total of 38 analyzed images). To compare TZ widths between subjects with RP and subjects with Usher syndrome, a two-tailed Mann-Whitney test was applied to both horizontal and vertical EZ widths.

Adaptive Optics Scanning Light Ophthalmoscopy

All subjects were imaged using a previously described confocal AOSLO.[14] In addition, 11 subjects were imaged using split-detector AOSLO.[32] Retinal image sequences were obtained using a 775-, 790-, or 796-nm superluminescent diode, subtending variable square fields of view (1°, 1.25°, 1.5°, 1.75°, or 2.0°). In the 11 subjects undergoing both confocal and split-detector AOSLO imaging, the confocal and split-detector image sequences were acquired simultaneously and were in perfect spatial register with each other. Foveal locations were sampled by instructing the subject to fixate on the corners or edges of the scanning raster, whereas parafoveal locations were examined using an adjustable internal fixation target, extending out to 10° eccentricity in both the temporal and superior directions. Two orthogonal imaging axes are used to facilitate alignment with clinical images and to adjust for rotational offsets between AOSLO and other modalities. The temporal and superior axes were chosen because of availability of normative cone density data in these regions,[53] and because (1) in our experience, the thinner retinal nerve fiber layer in the temporal direction provides for better imaging quality, whereas (2) imaging along the superior axis approaches the location of maximal rod density at approximately 12° superior eccentricity.[54]

To correct for distortions in the AOSLO retinal images due to the sinusoidal motion of the resonant optical scanner, distortion was first estimated from images of a Ronchi ruling. Image sequences (split-detector and/or confocal) were then resampled over a grid of equally spaced pixels. After "desinusoiding," the image sequences were manually inspected to identify reference frames with minimal distortion and maximal sharpness for subsequent registration using custom software.[55] When image sequences from both confocal and split-detector modalities were available, the reference frames were chosen from only one modality. The remaining frames in that modality were then registered to that reference frame by dividing each of the remaining frames in the image sequence into strips and aligning each strip to the location in the reference frame that maximizes the normalized cross-correlation.[55] The transforms from this registration process were then applied to corresponding image sequence acquired using the other modality. Once all frames were registered, a variable number of frames (~50) with the highest normalized cross-correlation to the reference frame were averaged to increase signal-to-noise ratio (SNR) and generate a final image from each image sequence. The size of the AOSLO image was determined by scaling the predicted visual angle for an eye with an axial length of 24 mm (291 μm/deg)[56] in proportion to the subject's measured axial length.

The AOSLO images were then manually assembled into a montage using Adobe Photoshop (Adobe Systems Incorporated, San Jose, CA, USA). In some cases, minor distortions between overlapping frames were corrected manually with rotational transformations. Using Photoshop, the resultant confocal and split-detector montages for each subject were scaled and aligned with color fundus images, HVF deviation maps, and the SD-OCT en face images. The foveal center was identified manually in both horizontal and vertical SD-OCT line scans, defined as the deepest point of the anatomic foveal pit. The position of the SD-OCT line scans (passing through the anatomic fovea) was determined by manually inspecting individual B-scans within the SD-OCT volumes. The position of the matching B-scan was then marked on the corresponding en face image, enabling precise comparison between SD-OCT features and those in the AOSLO montages.

Foveal and Parafoveal Cone Density Measurements and Statistical Analysis

For each subject, regions of interest (ROIs) used in cone counts were generated using a previously described method.[57] Foveal cone counts were estimated as close as possible to the anatomic foveal pit, the location of which was mapped onto the AOSLO montage using methods described above. In 15 montages, cones at the exact foveal center were obscured by poor image quality, and cones were counted at the nearest possible eccentricity. The average eccentricity at which foveal cones were counted was 0.15°, and the maximum eccentricity was 0.27° in one outlying case. Parafoveal cones were imaged and counted at approximately 0.65° eccentricity by instructing the subject to fixate on the top right corner of the imaging raster.

Cones were identified over a 55 × 55-μm sampling area at foveal and parafoveal locations using a custom semiautomated software that located cones based on analysis of local intensity maxima.[57] Non-waveguiding "dark" cones were not counted, and images were viewed on both linear and logarithmic scales to assist in identifying dimly reflecting cones. The count was then manually adjusted by a single observer (L.W.S.) who was masked to the clinical diagnosis (RP versus Usher syndrome) associated with the image. A final output in cones per square millimeter was calculated using the scaling factors described above. In each subject, the average of two measurements was taken at all locations. In two subjects, the measurements differed by more than 5% and a third tiebreaker measurement was taken. The outlier was discarded for purposes of analysis. Cone density measurements were compared with previously published normative values from nine healthy subjects.[53] To assess significance, 1-way analysis of variance (ANOVA) tests were performed for both foveal and parafoveal cone densities to generate an overall P value. Post hoc Tukey-Kramer multiple comparisons tests were then performed to determine the following inter-cohort P values: normal versus RP, normal versus Usher, and RP versus Usher.

Table 1. Characteristics and Foveal/Parafoveal Metrics of Subjects With RP

Subject	Age, y	Sex	Diagnosis	Identified Mutations	References and Predicted Pathogenicity (SIFT, PolyPhen-2, PROVEAN)	Eye	BCVA*	Foveal Sensitivity, dB†	Foveal Cones, mm²‡	Parafoveal Cones, mm²§
KS_10070||	56	F	Simplex RP	*RP1L1* c.190C>T; p.Leu64Phe	Novel (N/A, Prob. Damaging, Deleterious)	OD	20/16	30	80,905	70,218
				LCA5 c.2006G>T; p.Arg669Met	Novel (Damaging, Prob. Damaging, Deleterious)					
JC_1183	14	M	XLRP	*RPGR* c.379A>G; p.Arg127Gly	Sharon et al.[70]	OD	20/40	28	59,469	41,391
KS_10062||	15	M	XLRP	*RPGR* c.1374_1375insT; p.Val459Cys fs *4	Novel (N/A-frameshift)	OD	20/32	36	70,589	53,332
TC_0664¶	66	M	ARRP	*USH2A* c.10939+44C>T splice variant	Liquori et al.[59]	OD	20/30	34	107,597	57,710
			(Unilateral)	*USH2A* c.5858C>G; p.Ala1953Gly	McGee et al.[60]					
DH_10161||	49	F	ARRP	*USH2A* c.10073G>A; p.Cys3358Tyr	McGee et al.[60]	OS	20/16	36	103,464	60,884
				USH2A c.8016G>A; p.Leu2672Leu	Novel (Tolerated, N/A, Neutral)					
				BBS12 c.1237C>G; p.Leu413Val	Novel (Damaging, Prob. Damaging, Neutral)					
CK_10869||	65	M	ARRP	*EYS* c.9286_9295del10; p.Val3096Leu fs *28	Novel (N/A-frameshift)	OD	20/16	38	98,516	67,883
				EYS c.8206G>C; p.Ala2736Pro	Audo et al.[71]					
IE_0508#	48	F	ADRP	*RHO* c.68C>A; p.Pro23His	Bonilha et al.[72]	OD	20/20	36	130,335	68,063
TC_1176**	44	F	ADRP	*RP1* c.2029C>T; p.Arg677X	Bowne et al.[73]	OS	20/20	38	135,498	82,741
KS_10175||	51	M	ADRP	*RHO* c.173C>G; p.Thr58Arg	Dryja et al.[74]	OS	20/20	37	124,467	58,224
CK_10433||	78	M	ADRP	*RHO* c.68C>A; p.Pro23His	Dryja et al.[75]	OD	20/20	36	126,175	110,494
				USH2A c.3123C>A; p.His1041Gln	Reported, ClinVar Variation ID 48495[76]					
				CIB2 c.300_309del10; p.Glu100Asp fs *28	Novel (N/A-frameshift)					
				NPHP c.232T>C; p.Tyr78His	Reported, ClinVar Variation ID 167377[76]					
KS_10510||	50	F	ADRP	*NR2E3* c.166G>A; p.Gly56Arg	Schorderet and Escher[77]	OD	20/25	36	115,608	101,418
				CEP290 c.3853A>G; p.Lys1285Glu	Novel (Damaging, Prob. Damaging, Deleterious)					
				IFT140 c.2323G>A; p.Ala775Thr	Novel (Damaging, Prob. Damaging, Deleterious)					
				TRPM1 c.587C>T; p.Ser196Phe	Novel (Damaging, Prob. Damaging, Deleterious)					

SIFT 1.03 predicted pathogenicity: Damaging = tolerance index > 0.05; Tolerated = tolerance index ≤ 0.05. Polyphen-2 predicted pathogenicity: Prob. Damaging = 2 score > 0.950; Poss. Damaging = 0.900 < score ≤ 0.950; Benign = score ≤ 0.900; PROVEAN 1.1.3 predicted pathogenicity: Deleterious = δ score < −2.5; Neutral = δ score ≥ 2.5. Del, deletion; Eye, eye used for all measurements, assessments, imaging, and analysis; F, female; Fs, frameshift; Ins, insertion; M, male; X, stop codon (truncation); *(*n*), stop codon in *n* residues.

* Normal BCVA ≥ 20/25 (0.8).

† Normal foveal sensitivity ≥ 35 dB.

‡ Normal mean foveal cone density = 119,768 cones/mm².[53]

§ Normal mean parafoveal cone density (0.65° temporal eccentricity) = 78,721 cones/mm².[53]

|| All exons and immediately flanking introns of the following genes were examined: **KS_10062 & KS_10070**: *ABCA4, ABHD12, ADAM9, AIPL1, ALMS1, ARL6/BBS3, BBS1, BBS2, BBS4, BBS5, BBS7, BBS9, BBS10, BBS12, BEST1, C1QTNF5, C2orf71, C8orf37, CA4, CABP4, CACNA1F, CACNA2D4, CDH23, CDHR1, CEP290/BBS14, CERKL, CHM, CIB2/USH1J, CLRN1, CNGA1, CNGA3, CNGB1, CNGB3, CNNM4, CRB1, CRX, DFNB31, DHDDS, ELOVL4, EYS, FAM161A, FSCN2, GNAT1, GNAT2, GPR179, GPR98, GRK1, GRM6, GUCA1A, GUCA1B, GUCY2D, HARS, IDH3B, IMPDH1, IMPG2, INPP5E, IQCB1, KCNJ13, KCNV2, KLHL7, LCA5, LRAT, LRIT3, LZTFL1/BBS17, MAK, MERTK, MFRP, MKKS/BBS6, MKS1/BBS13, MYO7A, NMNAT1, NPHP1, NR2E3, NRL, NYX, OFD1, OPA1, OPA3, OTX2, PCDH15, PDE6A, PDE6B, PDE6C, PDE6G, PDE6H, PDZD7, PITPNM3, PRCD, PROM1, PRPF3, PRPF31, PRPF6, PRPF8, PRPH2/RDS, RAX2, RBP3, RD3, RDH12, RDH5, RGR, RHO, RIMS1, RLBP1, ROM1, RP1, RP1L1, RP2, RP9, RPE65, RPGR, RPGRIP1, RS1, SAG, SDCCAG8/BBS16, SEMA4A, SLC24A1, SNRNP200/ASCC3L1, SPATA7, TOPORS, TRIM32/BBS11, TRPM1, TTC8, TULP1, UNC119, USH1C, USH1G, USH2A, WDPCP/BBS15, ZNF513*; **KS_10175 & DH_10161**: all previous and *CYP4V2, PHYH*; **KS_10510 & CK_10433**: all previous and *ABCD1, AHI1, ARL13B, ARL2BP, ATF6, B9D1, B9D2, BBIP1, BCM, C21orf2, C5orf42, CC2D2A, CDH3, CEP41, CISD2, CKAP4, CLN13, CLN14, CLN3, CLN5, CLN6, CLN8, COH1, CSPP1, CTSD/CLN10, DGKQ, DHX38, DNAJC5/CLN4, DRAM2, DTHD1, EFEMP1, EMC1, FZD4, GDF6, GJB2, GJB6, GPR125, GRN/CLN11, HK1, IFT27, IFT140, IFT172, IMPG1, ITM2B, KIAA1549, KIF7, KIZ, LHON, LRP5, MFN2, MFSD8/CLN7, MMACHC, MVK, NDP, NEK2, NEUROD1, NPHP4, OAT, PDE6D, PEX1, PEX2, PEX3, PEX5, PEX6, PEX7, PEX10, PEX12, PEX13, PEX14, PEX16, PEX19, PEX26, PNPLA6, POC1B, PPT1/CLN1, PRPF4, RAB28, RBP4, RGS9, RGS9BP, RPGRIP1L, SLC7A14, TCTN1, TCTN2, TCTN3, TEAD1, TIMM8A, TIMP3, TMEM67, TMEM126A, TMEM138, TMEM216, TMEM231, TMEM237, TPP1/CLN2, TSPAN12, TTC21B, TTLL5, WDR19, WFS1, ZNF408, ZNF423/NPHP14*; **CK_10869**: all previous and *AMACR, ARL3, C12orf65, C1orf186, CEP164, CEP250, HGSNAT, HMX1, IFT81, MELAS, MIR204, NR2F1, OR2W3, PEX11B, PRPS1, RDH11, SLC4A7*.

¶ TC_0664 has two *USH2A* mutations that are in trans (reside on different chromosomes), as genetic testing of this subject's child reveals a single heterozygous *USH2A* c.5858C>G (p.Ala1953Gly) mutation. All exons and immediately flanking introns of the following genes were examined: *ABCA4, ASCC3L1, BEST1, C2ORF71, C8ORF37, CA4, CERKL, CLRN1, CNGA1, CNGB1, CRB1, CRX, DHDDS, EYS, FAM161A, FSCN2, GUCA1B, IDH3B, IMPDH1, IMPG2, KLHL7, LRAT, MAK, MERTK, NR2E3, NRL, OFD1, PDE6A, PDE6B, PDE6G, PRCD, PROM1, PRPF3, PRPF6, PRPF8, PRPF31, PRPH2, RBP3, RDH12, RGR, RHO, RLBP1, ROM1, RP1, RP2, RP9, RPE65, RPGR* (not including ORF15), *SAG, SEMA4A, SPATA7, TTC8, TOPORS, TULP1, USH2A, ZNP513, RS1, CHM*, and *C1QTNF5*.

All exons and immediately flanking introns of the following genes were examined: *C1QTNF5, RDS, RHO*, and *RP1*.

** TC_1176 is the son of a subject with clinically and genetically confirmed ADRP. In the subject, all exons and immediately flanking introns of the following genes were examined: *RP1*. In the subject's father, all exons and immediately flanking introns of the following genes were examined: *C1QTNF5, RDS, RHO*, and *RP1*.

Table 2. Characteristics and Foveal/Parafoveal Metrics of Subjects With Usher Syndrome

Subject	Age, y	Sex	Diagnosis	Identified Mutations	References and Predicted Pathogenicity (SIFT, PolyPhen-2, PROVEAN)	Eye	BCVA*	Foveal Sensitivity,† dB	Foveal Cones,‡ mm²	Parafoveal Cones,§ mm²
JC_1157||	7	F	Usher I	*MYO7A* c.397_398insC; p.His133Pro fs *7	Reported, ClinVar Variation ID 43229[76]	OD	20/40	33	73,293	38,494
				MYO7A c.4805G>A; p.Arg1602Gln	Liu et al.[78]					
MP_10137¶	9	M	Usher I	*MYO7A* splice variant IVS3-2A>G	Liu et al.[79]	OD	20/30	35	63,537	52,920
				MYO7A c.5967C>A; p.Tyr1989X	Novel (N/A–stop, N/A–stop, Deleterious)					
				MYO7A c.5866G>A; p.Val1956Ile	Reported, ClinVar Variation ID 43305[76]					
DW_0111#	29	F	Usher II	*USH2A* c.5877_delT; p.Ser1961Gln fs *6	Reported, ClinVar Variation ID 180092[76]	OD	20/30	29	50,569	36,568
				USH2A partial del exons 22-27	Novel (N/A - exon deletion)					
KS_0588#	34	M	Usher II	*USH2A* partial del exons 22-24	Baux et al.[80]	OD	20/25	37	74,613	54,028
				USH2A c.8682-9A>G splice variant	Dreyer et al.[81]					
				DFNB31 c.1148C>A; p.Thr383Asn	Reported, ClinVar Variation ID 163051[76]					
KS_10084**	28	F	Usher II	*USH2A* c.9842G>T; p.Cys3281Phe	Le Quesne Stabej et al. 2012[82]	OD	20/20	38	66,978	45,475
				USH2A c.3584G>T; p.Cys1195Phe	Reported, ClinVar Variation ID 179130					
				USH2A c.15017C>T; p.Thr5006Met	Novel (Damaging, Prob. Damaging, Neutral)					
JC_10158**	36	F	Usher II	*USH2A* c.2299delG; p.Glu767Ser fs *21	Eudy et al.[83]	OS	20/32	33	76,183	43,452
				USH2A c.5836C>T; p.Arg1946Stop	McGee et al.[60]					
JC_1088††	54	F	Usher III	*GPR98* c.17761T>C; p.Cys5921Arg	Novel (Damaging, Benign, Neutral)	OD	20/25	37	73,211	34,985
				GPR98 c.17996T>C; p.Leu5999Pro	Novel (Damaging, Prob. Damaging, Deleterious)					
KS_1077††	45	M	Usher III	*GPR98* c.17761T>C; p.Cys5921Arg	Novel (Damaging, Benign, Neutral)	OD	20/20	29	76,055	43,053
				GPR98 c.17996T>C; p.Leu5999Pro	Novel (Damaging, Prob. Damaging, Deleterious)					

SIFT 1.03 predicted pathogenicity: Damaging = tolerance index > 0.05; Tolerated = tolerance index ≤ 0.05. Polyphen-2 predicted pathogenicity: Prob. Damaging = 2 score > 0.950; Poss. Damaging = $0.900 <$ score ≤ 0.950; Benign = score ≤ 0.900; PROVEAN 1.1.3 predicted pathogenicity: Deleterious = δ score < -2.5; Neutral = δ score ≥ 2.5. Del, deletion; Eye, eye used for all measurements, assessments, imaging, and analysis; F, female; Fs, frameshift; Ins, insertion; M, male; X, stop codon (truncation); *(*n*), stop codon in *n* residues.

* Normal BCVA $\geq$ 20/25 (0.8).

† Normal foveal sensitivity $\geq$ 35 dB.

‡ Normal mean foveal cone density = 119,768 cones/mm².[53]

§ Normal mean parafoveal cone density (0.65° temporal eccentricity) = 78,721 cones/mm².[53]

|| Genetic information provided by subject. Analysis performed by Asper Labs.

¶ All exons and immediately flanking introns of the following genes were examined: *MYO7A*.

All exons and immediately flanking introns of the following genes were examined: *ABHD12, CDH23, CLRN1, DFNB31, GPR98, MYO7A, PCDH15, USH1C, USH1G, USH1J, USH2A,* and *USH3B*.

** All exons and immediately flanking introns of the following genes were examined: *ABHD12, CDH23, CLRN1, DFNB31, GPR98, MYO7A, PCDH15, PDZD7, USH1C, USH1G, USH1J, USH2A,* and *USH3B*.

†† These subjects are siblings. All exons and immediately flanking introns of the following genes were examined: *ABHD12, CDH23, CLRN1, DFNB31, GPR98, MYO7A, PCDH15, USH1C, USH1G, USH1J, USH2A,* and *USH3B*.

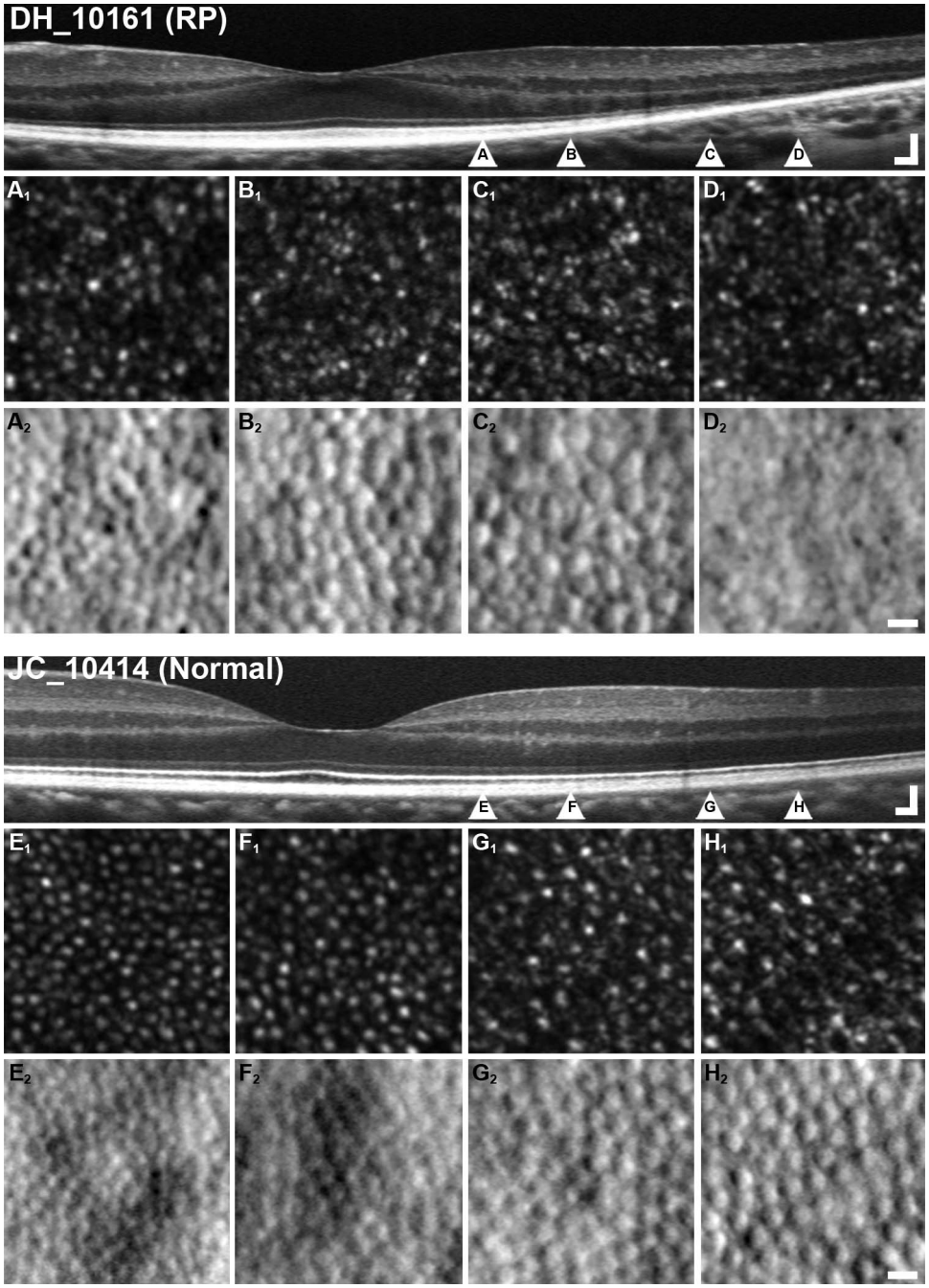

Figure 1. Adaptive optics scanning light ophthalmoscopy confocal and split-detector imaging reveals morphologic changes in diseased photoreceptors corresponding to SD-OCT findings. Images from two subjects (DH_10161, ARRP; JC_10414, normal control) are presented here. (*Top*) Representative images acquired from the left eye of DH_10161, a subject with RP. Nasal is toward the left and temporal is toward the right. (**A**) Point of IZ termination (662 μm from the fovea in this subject), (**B**) representative area of the transition zone between IZ and EZ terminations (1036 μm from the fovea), (**C**) point of EZ termination (1618 μm from the fovea), and (**D**) the point of ELM termination (1994 μm from the fovea). The AO images in small panels below correspond to the four locations indicated by labeled *arrowheads* on the corresponding SD-OCT; *top panels* are confocal images, whereas *bottom panels* are split-detector images. Pretransition SD-OCT shows intact IZ and EZ bands (**A**). Confocal AOSLO (**A_1**) shows non-waveguiding cones that correspond to relatively healthy-appearing cone inner segments on split-detector imaging (**A_2**). Transition-zone SD-OCT (**B**) shows loss of IZ band and decay of EZ band, which corresponds to loss of the IZ peak and a smaller EZ peak on LRP. Confocal AOSLO (**B_1**) shows aberrant cones that have lost their approximately Gaussian intensity profile and instead appear as small clusters of bright dots. Examination of the split detector image (**B_2**) shows intact but enlarged cone inner segments. Past the point of EZ termination on SD-OCT corresponding to loss of EZ peak on LRP (**C**), confocal images (**C_1**) show non-waveguiding cones, as well as indistinct signals that may correspond to debris, rods, or cones. However, examination of split detector images (**C_2**) allows for distinction between debris/rods and enlarged remnant cone inner segments. Finally, past the point of ELM termination on SD-OCT corresponding to loss of the ELM peak on LRP (**D**), confocal images (**D_1**) show uninterpretable signals that look very similar to the confocal images seen in **C_1**. In contrast, split-detector images (**D_2**) clearly show loss of nearly all remnant cone structure at this point. (*Bottom*) Representative images acquired from the left eye of JC_10414, a healthy subject. Nasal is toward the left and temporal is toward the right. Both SD-OCT and AO images are set to the same scale as the corresponding images of DH_10184, and the same retinal locations (662, 1036, 1618, and 1994 μm) are presented. Note intact IZ, EZ, and ELM bands on SD-OCT throughout imaged area, as well as punctate, reflective cones on confocal AOSLO imaging corresponding to distinct inner segments on split-detector AOSLO imaging. *Scale bars*: SD-OCT images = 100 μm; AOSLO images = 10 μm.

Investigative Ophthalmology & Visual Science

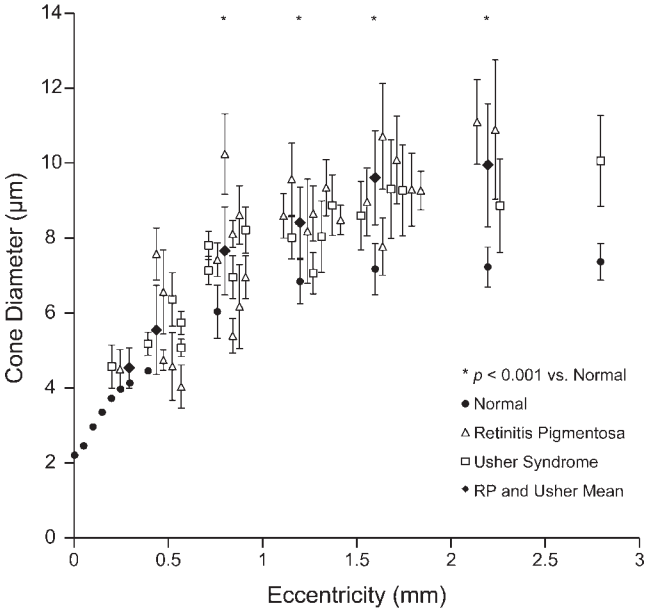

Figure 2. Cone diameters are significantly increased in the transition zones of subjects with RP and Usher syndrome**.** Cone diameters in micrometers in affected and healthy subjects are plotted against retinal location (temporal to the fovea). Mean cone diameters were manually measured using AOSLO split-detector images of 16 healthy subjects, 4 subjects with RP, and 4 subjects with Usher syndrome (see Methods for details). Intrasubject means, derived from 10 measurements at each eccentricity in a single subject, are presented as *open triangles* (RP) and *open squares* (Usher syndrome). Pooled intersubject means, derived from the pooled measurements at each eccentricity in all subjects, are represented by *filled diamonds* (RP and Usher) and *filled circles* (normal controls). Overlapping data points are displaced horizontally for easier visualization. *Error bars* denote 1 SD. Normal values at less than 500 μm (approximately 1.72°) eccentricity are measured from histologic samples[32]; due to small sample size, no SD is provided. Note that in three of seven cases at 800 μm (2.75°) eccentricity, five of eight cases at 1200 μm (4.10°) eccentricity, six of seven cases at 1600 μm (5.50°) eccentricity, and four of four cases at 2200 (7.56°) and 2800 μm (9.62°) eccentricity, RP and Usher syndrome intrasubject mean diameters are >2 SDs greater than normal mean, and thus exceed the 95th percentile of normal cone diameter. At 800-, 1200-, 1600-, and 2200-μm eccentricities, where both normal intersubject mean cone diameters and affected intersubject mean cone diameters were available, mean cone diameter was significantly increased in RP and Usher syndrome (* indicates $P < 0.001$ using Student's *t*-test).

Transition Zone Cone Density Measurements

Due to aberrant cone reflectivity on confocal imaging (see Introduction), it was necessary to count cones in the transition zone using split-detector AOSLO images. For each of the 11 subjects with split-detector images, six 55 × 55-μm ROIs along the temporal meridian were cropped from their AOSLO montages. The location of each ROI was selected to correspond to (1) the point of IZ dropout on the aligned SD-OCT, (2) at the point of EZ dropout, and (3–6) locations at 20%, 40%, 60%, and 80% of the distance between point 1 and point 2. Within each ROI, cones were manually identified by a single observer (L.W.S.) who was masked to the identity of the subject. Two measurements were taken per ROI and averaged. Measurements that differed by more than 5% triggered a third tiebreaker measurement, after which the outlier was discarded.

Because of varying degrees of pathology, actual temporal eccentricities for each ROI varied greatly between subjects. To normalize data across subjects, each cone density measurement was converted to a percentage of the cone density at the beginning of the TZ (defined as the point of IZ dropout) for that subject. Each ROI location was then converted to a percentage of the total distance between the start and end of the TZ for that subject; that is, the distance between the point of IZ dropout and the point of ELM-RPE merge.

Transition Zone Cone Diameter Measurements

The diameters of cone inner segments within the TZ were also measured using split-detector AOSLO images. For each subject, each of the following temporal eccentricities in the imaged eye was assessed for adequate image quality: 291, 435, 800, 1200, 1600, 2200, and 2800 μm (corresponding to ∼1°, 1.5°, 2.75°, 4.10°, 5.50°, 7.56°, and 9.62°). In regions where pathology had eliminated all discernible cone structure, ROIs were not selected. In eight subjects, resolution of cone inner segments with split-detector AOSLO at 291 μm was not possible. In one subject, split-detector imaging was not performed at 291, 435, or 800 μm. At each area deemed acceptable for cone diameter measurement, 0.5 × 0.5° ROIs were generated. The final sample sizes were as follows: $N = 2$ at 291 μm, $N = 10$ at 435 μm, $N = 10$ at 800 μm, $N = 10$ at 1200 μm, $N = 8$ at 1600 μm, $N = 3$ at 2200 μm, and $N = 1$ at 2800 μm.

For comparison, cone diameters were measured using split-detector AOSLO images at approximately 800, 1200, 1600, 2200, and 2800 μm temporal to the fovea in 16 healthy subjects. In normal subjects, tight foveal cone packing precluded resolution and measurement of cone inner segments at eccentricities less than 800 μm. In some normal subjects, certain eccentricities were unusable due to poor image quality. Thus, final sample sizes at each ROI were as follows: $N = 12$ at 800 μm, $N = 16$ at 1200 μm, $N = 15$ at 1600 μm, $N = 16$ at 2200 μm, and $N = 15$ at 2800 μm. For each subject, measurements were taken from one eye. In addition, normative data derived from previously published histologic studies[32] were also used for comparison.

For the 16 healthy subjects and 11 subjects with RP or Usher syndrome, 10 inner segments were arbitrarily selected from each ROI and manually measured by a single observer (M.C.R.) using ImageJ.[58] Each cell was measured twice using two orthogonal lines placed at the center of the cell, with the cell diameter recorded as the mean length of the two lines. The mean cell diameter at each eccentricity was calculated by averaging all cell diameters recorded at that eccentricity in all subjects at which that eccentricity was measured. Diameters at a given eccentricity were not binned by subject to preserve as much information as possible about both inter- and intrasubject variability. Similarly, an SD was calculated from the raw mean of all cell diameters at each eccentricity without binning by subject. Where mean cell diameters were available for both affected and healthy subjects, significance was assessed using the Student *t*-test for two independent means. Corresponding two-tailed *P* values were generated using the *t*-score, and degrees of freedom was calculated as independent samples.

Results

Subject Demographics and Clinical Data

A brief summary of subject demographics, clinical characteristics, and genetic profiles is provided in Tables 1 and 2, with a

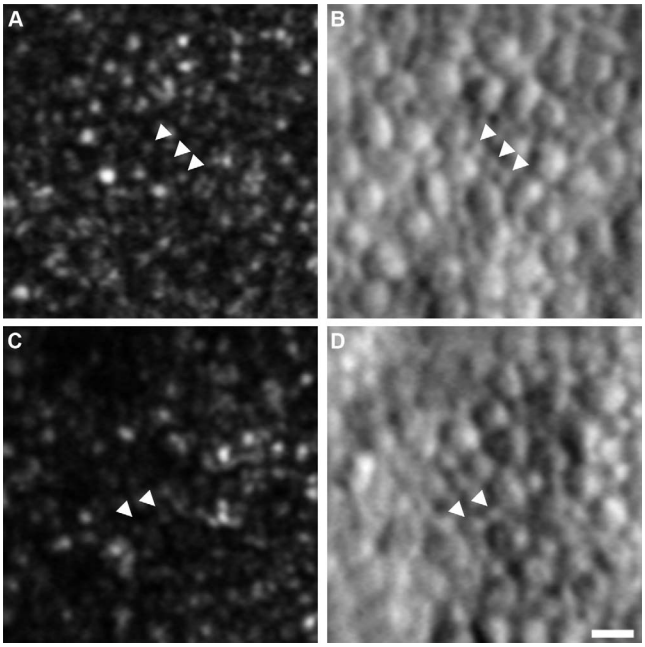

FIGURE 3. Rods can be visualized and distinguished from cones with AOSLO split-detector imaging. Occasionally, we were able to resolve rod structure on split-detector imaging. These images were captured from the temporal parafovea of DH_10161. (**A**,**B**) Confocal and split-detector images of the same field of view at approximately 1570-μm eccentricity. (**C**,**D**) Similarly acquired images at approximately 1995-μm eccentricity. In the confocal modality (**A**,**C**), rods can appear indistinguishable from surrounding cone signals, particularly where cone reflectivity is no longer Gaussian. However, on split-detector imaging (**B**,**D**), the distinction between small rods and much larger cones can be easily made. *Scale bar*: 10 μm.

complete analysis of genetic results provided in Supplementary Text S1. One subject, TC_0664, exhibited a unilateral case of ARRP. Genetic testing revealed two previously reported disease-causing mutations in *USH2A*: c.10939+44C > T splice variant[59] and c.5858C > G; p.Ala1953Gly.[60] Genetic testing of the subject's son revealed a heterozygous *USH2A* c.5858C > G; p.Ala1953Gly mutation, consistent with the *USH2A* mutations in TC_0664 being in trans.

Classification of subjects with RP was based on clinical symptoms, inheritance pattern, and/or genotype. Mean BCVA for all subjects with RP was 0.98, which corresponds to approximately 20/20 vision (normal ≥ 0.8 or 20/25), and mean foveal sensitivity was 35 dB (normal ≥ 35). By subtype, mean BCVA was 1.25 for simplex RP, 0.56 for XLRP, 1.06 for ARRP, and 0.96 for ADRP. Mean foveal sensitivity was 30 dB for simplex RP, 32 dB for XLRP, 36 dB for ARRP, and 37 dB for ADRP. Five subjects were found to have one or more previously reported mutations, two were found to have one or more novel mutations, and the remaining four subjects had both novel and previously published/reported mutations (Table 1).

Classification of subjects with Usher syndrome was based on clinical symptoms, genotype, and/or age of onset. Mean BCVA for all subjects with Usher syndrome was 0.76, which corresponds to approximately 20/26 vision. Mean foveal sensitivity was 33.88 dB. By subtype, mean BCVA was 0.58 for Usher type I, 0.77 for Usher type II, 0.90 for Usher III, and 0.29 for suspected Usher; mean foveal sensitivity was 34 dB for Usher type I, 34.5 dB for Usher type II, 33 dB for Usher type III, and 27 for suspected Usher. Four subjects were found to have one or more previously published/reported mutations, two were found to have one or more novel mutations, and the remaining two subjects had both novel and previously published/reported mutations (Table 2).

Ellipsoid Zone Band Width From OCT

Horizontal and vertical EZ widths were measured in all 19 subjects using SD-OCT images. All horizontal SD-OCT images are shown in Supplementary Figure S1. Horizontal widths ranged from 1401 (KS_10175) to 4894 μm (JC_1088); vertical widths ranged from 1213 (KS_10175) to 4267 μm (TC_0664). In three subjects (TC_0644, KS_1077, and CK_10869), the EZ extended beyond the scanning window in at least one direction on SD-OCT scan. As such, determination of the extent of retained EZ was not possible for these three subjects. For all subjects in whom a complete EZ width could be measured, the mean horizontal EZ width was 2797 μm in RP and 3145 μm in Usher syndrome. The mean vertical EZ width was 2454 μm in RP and 2416 μm in Usher syndrome. Mann-Whitney tests determined no significant difference in EZ widths in RP versus Usher cohorts for either horizontal ($U = 26$ and $P = 0.60$, critical $U = 12$ at $P \leq 0.05$) or vertical measurements ($U = 33$ and $P = 0.88$, critical $U = 14$ at $P \leq 0.05$). These results are consistent with HVF results indicating no appreciable difference in visual field constriction between Usher and RP cohorts (data not shown).

Cone Structure in the TZ

Figure 1 shows OCT and AO images of the TZ in a subject with RP and a normal subject for comparison. Supplementary Figure S2 shows OCT and AO images of the TZ in a subject with Usher syndrome. In both RP and Usher syndrome, confocal AOSLO within the TZ (defined as the region between the loss of the IZ peak to the loss of the EZ peak on LRP analysis) shows numerous cones that appear as dark gaps in the foveal cone mosaic. However, the TZ also contains cones with abnormal waveguiding profiles (Figs. $1B_1$, $1C_1$, $1D_1$). Although pre-TZ cones typically appear as Gaussian spots on confocal AOSLO, cones in areas corresponding to IZ disruption often have an altered appearance (either a single dim spot or small clusters of bright spots). Although dark cones are increasingly common at greater eccentricities, there is no sharp distinction on confocal AOSLO between areas with and without an intact EZ band on SD-OCT. In addition, across the TZ (Figs. $1A_1$–$1D_1$), it is difficult to discern cone versus rod structure using confocal AOSLO imagery.

Although the confocal signal is generally uninterpretable throughout the TZ, split-detector AOSLO imaging allows unambiguous identification of cone inner segments. The remnant cone inner segments in the TZ were significantly enlarged compared with healthy controls at nearly all eccentricities sampled (Fig. 2). In one case (DH_10161), rod inner segments located between enlarged cone inner segments could also be clearly visualized using the split-detector imaging at several locations within the TZ (Fig. 3). The split-detector AOSLO images revealed remnant cone inner segment structure throughout the TZ in all subjects with no sharp distinction between the appearance of cone inner segments in areas corresponding to presence versus loss of the IZ band, nor presence versus loss of the EZ band on SD-OCT (Figs. $1A_2$ versus $1B_2$ versus $1C_2$). Interestingly, cone inner segments persist past the point of EZ band dropout, although they become sparser with increasing eccentricity. By the point at which the ELM collapses onto the RPE, cone inner segments have generally disappeared

Investigative Ophthalmology & Visual Science

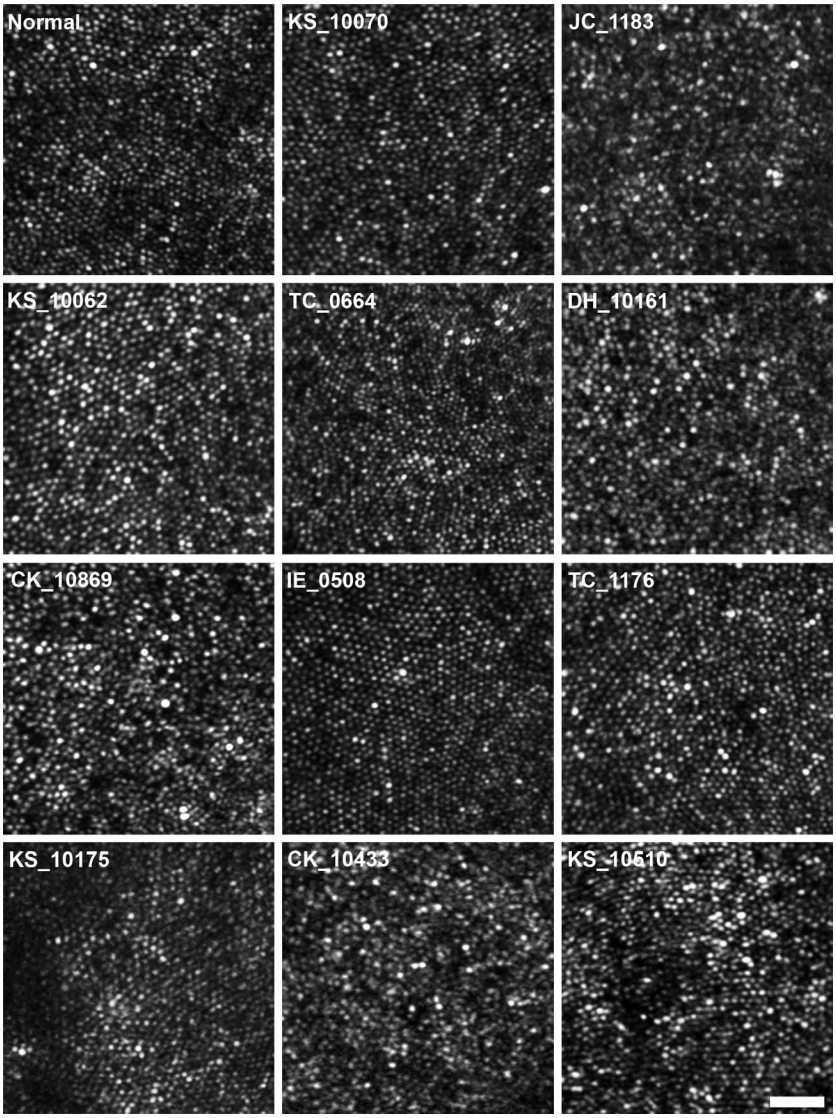

Figure 4. Parafoveal cone mosaics in RP. Shown are $0.5 \times 0.5°$ field of view images of parafoveal cone mosaics (approximately 0.65° eccentricity) in 1 healthy control (AD_10252) and 11 subjects with RP. Subjects are arranged in the same order as listed in Table 1: simplex RP (KS_10070), XLRP (JC_1183 and KS_10062), ARRP (TC_0664, DH_10161, and CK_10869), and ADRP (IE_0508, TC_1176, KS_10175, CK_10433, and KS_10510). *Scale bar*: 25 μm.

altogether (Fig. $1D_2$). We mapped cone density across the TZ for all 11 subjects (Supplementary Fig. S3), observing significant variability in the rate of falloff in cone density. For example, normalizing for differences in the absolute size of the TZ and eccentricity at which the TZ began in each subject, we examined the cone density at 40% of the distance across the TZ (relative to the TZ start) and found a 27.6%–62.6% decrease from cone density at TZ start. At 60% of the distance, we observed a 42.7%–70.2% decrease. When looking at the entire TZ, the slope of the cone density versus retinal eccentricity function was steeper than that expected based on normal topographical changes in the cone mosaic (Supplementary Fig. S3). Whether this is due to increased rod numbers in the perifovea accelerating cone loss or simply reflects the temporal progression of the condition is unclear. Regardless, it will be interesting to monitor these measurements over time to more accurately capture the rate of cone loss in RP and Usher syndrome.

Foveal and Parafoveal Cone Density in Usher Syndrome Versus Retinitis Pigmentosa

Figures 4 and 5 show representative confocal AOSLO images of parafoveal cone mosaics from all subjects with RP and Usher syndrome, respectively. Individual cone density values measured from confocal AOSLO images are provided in Tables 1 and 2. Cone counts were pooled by diagnosis (RP versus Usher syndrome) to generate mean cone densities, SDs, and 95% confidence intervals (CIs), which were then compared with mean cone densities in healthy subjects published by Wilk et al.[53]

As shown in Figure 6, mean foveal cone density measured at a mean eccentricity of 0.15° was 100,901 cones/mm^2 (95% CI, ±20,312 cones/mm^2) in the subjects with RP. This is not significantly different ($P > 0.05$) from normative values published by Wilk et al., who reported cone density at 43.5 μm (approximately 0.15°) eccentricity to be 115,087 cones/mm^2 (95% CI, ±20,311 cones/mm^2).[53] In the subjects with

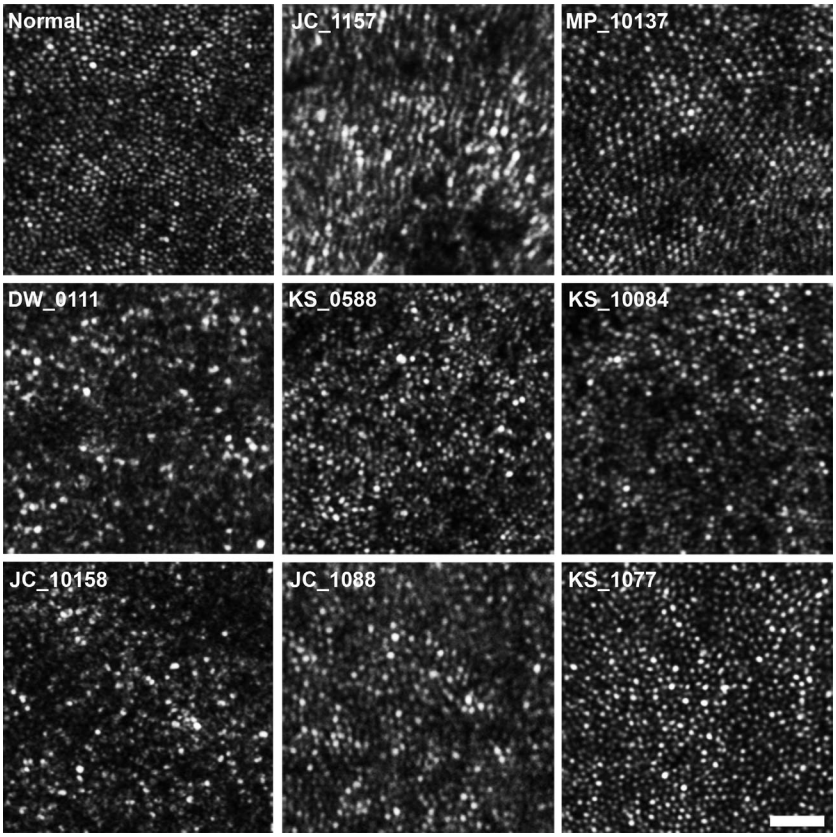

Figure 5. Parafoveal cone mosaics in Usher syndrome. Shown are $0.5 \times 0.5^\circ$ field of view images of the parafoveal cone mosaics (approximately 0.65° eccentricity) in one healthy subject (AD_10252) and eight subjects with Usher syndrome. Subjects are arranged in the same order as listed in Table 2: Usher type I (JC_1157 and MP_10137), Usher type II (DW_0111, KS_0588, KS_10084, and JC_10158), and Usher type III (JC_1088 and KS_1077). Note relatively more irregular cone spacing, sparser cones, and increased numbers of dark (non-waveguiding) cones in these parafoveal images compared with those from patients with RP (Figure 4). *Scale bar*: 25 μm.

Usher syndrome, mean foveal cone density was 69,305 cones/mm^2 (95% CI, ±5656 cones/mm^2; Fig. 6), which was significantly reduced compared with both the normal ($P < 0.01$) and RP groups ($P = 0.05$).

Mean parafoveal cone densities measured at a mean eccentricity of 0.65° are also shown in Figure 6. Subjects with RP had a mean density of 71,055 cones/mm^2 (95% CI, ±11,701 cones/mm^2), which was not significantly different from the normal value of 78,721 cones/mm^2 (95% CI, ±21,795 cones/mm^2; $P = 0.05$) For the subjects with Usher syndrome, the mean parafoveal cone density was 43,621 cones/mm^2 (95% CI, ±4471 cones/mm^2), which is significantly reduced compared with normal ($P = 0.01$) and RP ($P = 0.05$).

Figure 7 shows representative parafoveal images from two subjects with Usher syndrome type II. In confocal AOSLO images (Figs. 7A, 7C), numerous cones appear dark, similar to those in Figure 1. Arrowheads indicate a series of such dark cones. In contrast, split-detector AOSLO images reveal cone inner segments (small circular mounds in Figs. 7B and 7D) at the same labeled locations, confirming the presence of remnant cone structure within the dark areas of the confocal AOSLO images.

Foveal Cone Density and Visual Function Metrics

Best-corrected visual acuity from all subjects is plotted against their corresponding foveal cone density in Figure 8A. Pearson's r values calculated for BCVA versus foveal cone density was 0.601 ($P = 0.007$), indicating a significant correlation. A logarithmic best-fit line was plotted using values from both subsets of subjects, which has an R^2 value of 0.388, indicating moderate goodness-of-fit. Normal BCVA was defined as 20/25 and above (0.8 and above on the decimal scale) and is indicated by a horizontal dashed line in Figure 8A. The plotted best-fit line crosses this threshold at 71,615 cones/mm^2, which is reduced by 37.73% from mean normal foveal cone density.

Pearson's r values calculated for foveal sensitivity versus foveal cone density was 0.520 ($P = 0.023$), indicating a significant correlation. A best-fit logarithmic line plotted using values from all subjects has an R^2 value of 0.292, indicating modest goodness-of-fit. Normal foveal sensitivity is defined as 35 dB and above and is indicated by a horizontal dashed line in Figure 8B. The plotted best-fit curve crosses this threshold at 90,859 cones/mm^2, which is reduced by 20.99% from normal foveal cone density. This suggests that foveal sensitivity may be a more sensitive measure of disease severity than visual acuity.

Discussion

Owing to the emergence of high-resolution retinal imaging tools, there has been increased interest in examining retinal anatomy in RP and allied disorders. Previous groups have reported increased cone spacing and/or decreased cone density in subjects with RP.[21,24–27,29–31] In our cohort, we found a small but statistically insignificant decrease in the

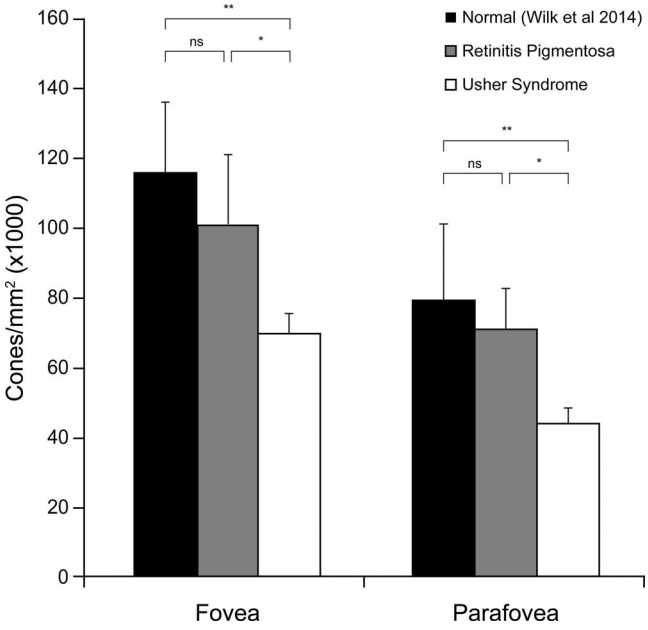

Figure 6. Foveal and parafoveal cone density is significantly decreased in Usher syndrome. Shown are foveal and parafoveal cone densities for healthy subjects, subjects with RP, and subjects with Usher syndrome. Foveal cone densities were measured at 0.15° mean eccentricity, whereas parafoveal cone densities were measured at 0.65° mean eccentricity. *Error bars* denote 95% CIs. At foveal and parafoveal locations, cone density was significantly decreased in Usher syndrome compared with both healthy subjects ($P < 0.01$, indicated by **) and subjects with RP ($P < 0.05$, indicated by *). Subjects with RP, however, did not have a significantly decreased cone density foveally or parafoveally as compared with healthy subjects ($P > 0.05$, indicated by ns).

density of waveguiding foveal cones in RP. In contrast, a significant decrease in foveal cone density was seen in subjects with Usher syndrome. We also showed that the reduced density in Usher syndrome was a result of a reduced number of normal waveguiding cones, as the dark regions in the image often contained remnant inner segment structure. These findings may be explained by the different molecular pathways involved in RP versus Usher syndrome: for example, changes in outer segment proteins may not impact cone waveguiding as much as proteins localized to the connecting cilium. However, due to sample size limitations, we were unable to correlate foveal cone densities with potential confounds such as subject age, length of disease, and/or genotype. Future studies addressing these subgroups would add valuable information. Regardless of the origin of these observed differences, they illustrate that caution should be used in interpreting confocal AOSLO images to infer the number of residual cone photoreceptors in subjects with active retinal degeneration.

The observed reductions in foveal cone density were frequently "subclinical," as cone density in RP and Usher syndrome could be reduced by nearly 38% from normal before BCVA declined to clinically abnormal ranges (20/25 or less). This finding agrees with previous work demonstrating significant differences in foveal cone mosaics of RP-affected subjects even in the setting of normal visual acuity.[21,27] However, waveguiding foveal cone density was found to significantly correlate with visual function throughout both normal and abnormal ranges of BCVA and foveal sensitivity. This correlation of foveal photoreceptor anatomy on AOSLO to measures of visual function despite no visible foveal change on SD-OCT is particularly interesting in light of previous studies showing abnormal functional metrics despite normal-appearing retinal anatomy on OCT.[4,13] Taken together, these findings speak to the emerging role of AOSLO in detecting changes in photoreceptor structure that are not detectable with standard clinical tools.

Additionally, the correlation of foveal waveguiding cone density to visual acuity raises the interesting question of whether waveguiding reflectivity in cones can be used as an implicit measure of function. Recent work addressing the issue used AO microperimetry to test the perceptual thresholds of single cones in healthy subjects and noted no significant decrease in sensitivity of poorly reflective cones.[47] This suggests that cone reflectivity, at least in healthy subjects, may be unrelated to function. In disease, this is not necessarily the case. Makous et al. used AO microperimetry to show a 28% decrease in sensitivity in a retina with approximately 30% loss of normal waveguiding cones.[61] Additionally, a number of reports have documented diminished cone reflectivity on confocal AOSLO in patients with clinically reduced visual function,[18,20,25,33,39–41] and one case noted recovery of normal reflectivity with concurrent functional improvement.[33] Despite this, the ability to infer cone function from reflectivity is confounded by the fact that cones can spontaneously recover normal reflectivity without documented change in function[20,62] and that cone reflectivity can vary over time in RP and allied disorders (Supplementary Fig. S4). In the future, applying AOSLO microperimetry technology to individuals with retinal disease may help resolve the functional status of cones with altered waveguide properties.

The integrity of the EZ (or IS/OS) has received substantial attention within RP studies, specifically concerning the extent of retained/intact EZ in the central retina (i.e., "EZ width"). This is due in part to the relative ease of determining the presence or absence of the EZ, the general good correspondence between the edge of cone-driven visual field sensitivity, and the EZ contour,[6] as well as the excellent reliability of the measurement.[63] As such, EZ width has been proposed as a possible anatomical end point for RP clinical trials.[63,64] However, as shown here, the integrity of the EZ by itself cannot be used to discriminate between rod and cone photoreceptor structure, at least with the resolution offered by existing OCTs. Using confocal AOSLO, we observed significant disruption of the cone mosaic in areas of an intact EZ, although there was relatively good correspondence between the disruption of the IZ band and disruption of the cone mosaic, consistent with previous results showing that confocal reflectivity corresponds closely to IZ band integrity.[50,65] In addition, we documented remnant cone inner segment structure with split-detector AOSLO beyond the point of EZ termination: in fact, inner segments were observed until the point of ELM collapse. Recent work in patients with macular telangiectasia type 2 has shown that EZ (or IS/OS) layer intensity can spontaneously recover in areas underlying a preserved ELM.[62] Although EZ width may in fact allow accurate tracking of disease progression in RP, the extent of preserved ELM may be a better predictor of the extent of cone recovery that might be possible in these patients with therapeutic intervention.

Although confocal AOSLO has been a remarkable tool for examining cone photoreceptor structure in RP and other conditions, the present study highlights a significant limitation for interpreting such images. This is due to its inherent reliance on intact cone morphology to facilitate proper waveguiding of incident light used for imaging. The

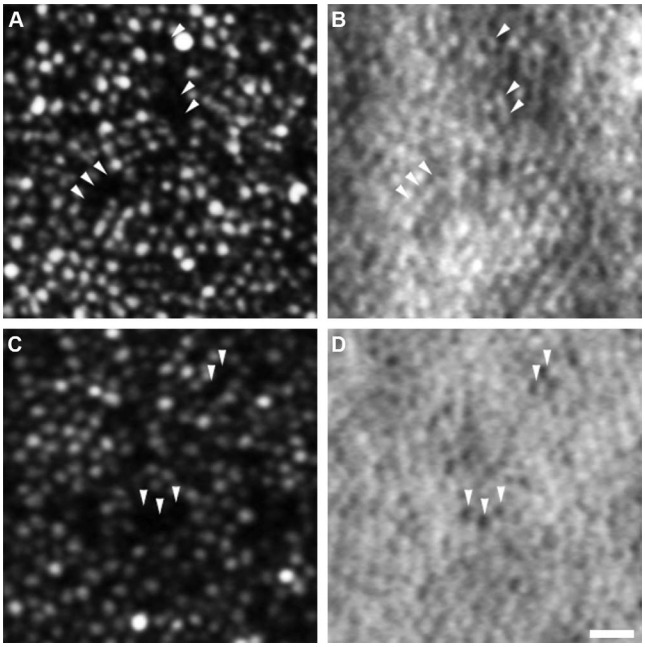

Figure 7. Non-waveguiding parafoveal cones with intact inner segments are visualized with the split-detector. Pictured here are confocal and split-detector images of 0.25 × 0.25° regions of the parafovea at approximately 0.65° in two subjects with Usher syndrome type II (KS_0588 and KS_10084). (**A**,**C**) Confocal AOSLO detects light waveguided through healthy cone photoreceptors, which typically appear as single brightly reflective spots. In contrast, cones with diseased outer segments or cones that are altogether absent appear dark in the parafovea. Several clusters of dark cones are indicated by *arrowheads*. The confocal modality cannot ascertain whether these cones merely have altered waveguiding or are altogether missing. (**B**,**D**) Split-detector AOSLO detects light scattered from cone inner segments and is thus able to differentiate between a cone with an altered outer segment and an entirely absent cone. The same clusters of cones in **A** and **B** are indicated by *arrowheads*. It is apparent that these cones, although non-waveguiding, still have remaining inner segment structure. *Scale bar*: 12.5 μm.

complementary split-detector modality provides a method of unambiguously identifying cone inner segments even in advanced disease states, allowing for a better understanding of photoreceptor structure in RP and Usher syndrome. Indeed, the mean diameters of cone inner segments were increased throughout the TZs of our subjects, consistent with alterations in photoreceptor morphology that disrupt cone waveguiding.[38,66,67] In addition, split-detector images allows for more accurate measurements of cone mosaic density, geometry, and inner segment diameter. Current cone identification tools take advantage of the expected Gaussian profile of cones seen in confocal AOSLO imagery,[57,68,69] which becomes problematic in the parafoveal/perifoveal retina where the multimodal reflectivity profile from a single cone can resemble a small cluster of rods. Such altered reflectivity profiles would degrade the accuracy of existing image analysis tools. Despite these limitations, confocal AOSLO allows better resolution of foveal cones and rods than split detection. Thus, it should be stressed that these AOSLO modalities are complementary and not competing. In fact, by combining split-detector and confocal modalities, it is possible to disambiguate whether a cone is absent, present but non-waveguiding, present but aberrantly waveguiding, or grossly normal. This ability to reliably discrim-

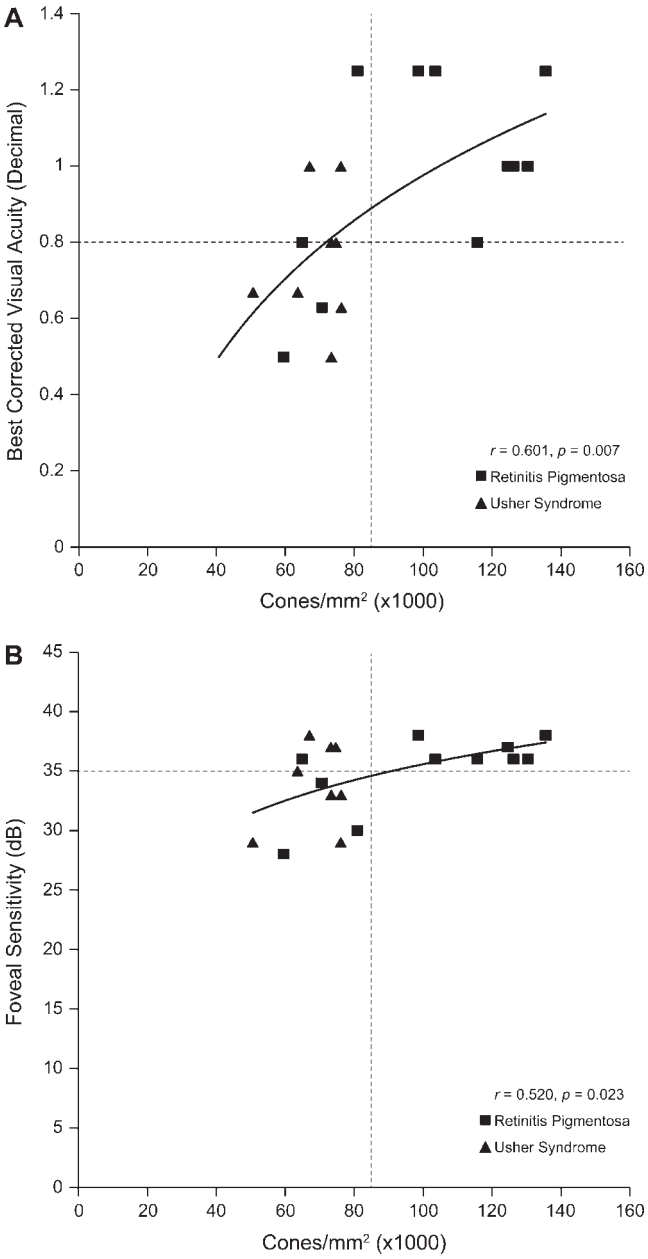

Figure 8. Visual function metrics correlated to foveal cone density. Subjects with RP are represented by *squares*, whereas subjects with Usher syndrome are represented by *triangles*. (**A**) Best-corrected visual acuity as a function of foveal cone density. Best-corrected visual acuity measured by ETDRS and converted to decimal notation is plotted as a function of cone density measured at approximately 0°–0.2° eccentricity. Pearson's correlation, $r = 0.601$ ($P = 0.006$). A least-squares logarithmic regression curve was generated ($R^2 = 0.388$). *Horizontal dashed line* represents nominally normal visual acuity, 20/25 (0.8), and above. (**B**) Foveal sensitivity (dB) as a function of foveal cone density. Foveal sensitivity measured by Humphrey 10-2 automated visual field testing is plotted as a function of cone density measured at approximately 0°–0.20° eccentricity. Pearson's correlation, $r = 0.520$ ($P = 0.023$). A least-squares logarithmic regression curve was generated ($R^2 = 0.292$). *Horizontal dashed line* represents nominally normal foveal sensitivity, 35 dB and above. *Vertical dashed lines* represent the lowest normal foveal cone density previously reported in the literature[53]: 84,733 cones/mm^2.

inate between a diseased cone and an absent cone may become increasingly important in the context of utilizing AOSLO for longitudinal monitoring of photoreceptor structure in subjects receiving experimental treatments for their retinal degeneration. It will be important to incorporate AO-based functional measurements[47] with these structural measurements to provide a more comprehensive picture of cone health in these retinas.

Acknowledgments

The authors thank Mara Goldberg, Brian Higgins, Emily J. Patterson, Alexander Salmon, Christine M. Skumatz, Phyllis Summerfelt, Brandon Wilk, Melissa Wilk, and Vesper Williams for their invaluable assistance and for innumerable helpful discussions.

Supported by National Institute of General Medical Sciences, National Institutes of Health, Award T32GM080202 and National Eye Institute, National Institutes of Health, Awards P30EY001931, R01EY017607, U01EY025477, T32EY014537, and K08EY021186. Additional support comes from the Richard O. Schultz, MD/Ruth Works Professorship, The Edward N. & Della L. Thome Memorial Foundation, Foundation Fighting Blindness, unrestricted departmental grants from Research to Prevent Blindness (MCW and CEI), the Thomas M. Aaberg Sr Retina Research Fund, the Gene and Ruth Posner Foundation, and the R.D. and Linda Peters Foundation. MP is the recipient of a Career Development award from Research to Prevent Blindness and an Early Career Development award from Foundation Fighting Blindness (CD-NMT-0914-0659-OHSU).

The content is solely the responsibility of the authors and does not necessarily represent the official views of the National Institutes of Health. This investigation was conducted in part in a facility constructed with support from the Research Facilities Improvement Program; grant number C06RR016511 from the National Center for Research Resources, NIH.

Disclosure: **L.W. Sun,** None; **R.D. Johnson,** None; **C.S. Langlo,** None; **R.F. Cooper,** None; **M.M. Razeen,** None; **M.C. Russillo,** None; **A. Dubra**, None; **T.B. Connor Jr,** None; **D.P. Han,** None; **M.E. Pennesi,** Sucampo Pharmaceuticals (C), ISIS Pharmaceuticals (C), AGTC (F), Sanofi (F); **C.N. Kay**, AGTC (C, F); **D.V. Weinberg,** None; **K.E. Stepien,** None; **J. Carroll,** AGTC (F)

References

1. Hood DC, Lazow MA, Locke KG, Greenstein VC, Birch DG. The transition zone between healthy and diseased retina in patients with retinitis pigmentosa. *Invest Ophthalmol Vis Sci*. 2011;52:101–108.
2. Fischer MD, Fleischhauer JC, Gillies MC, Sutter FK, Helbig H, Barthelmes D. A new method to monitor visual field defects caused by photoreceptor degeneration by quantitative optical coherence tomography. *Invest Ophthalmol Vis Sci*. 2008;49:3617–3621.
3. Jacobson SG, Aleman TS, Sumaroka A, et al. Disease boundaries in the retina of patients with Usher syndrome caused by MYO7A gene mutations. *Invest Ophthalmol Vis Sci*. 2009;50:1886–1894.
4. Dale EA, Hood DC, Greenstein VC, Odel JG. A comparison of multifocal ERG and frequency domain OCT changes in patients with abnormalities of the retina. *Doc Ophthalmol*. 2010;120:175–186.
5. Rangaswamy NV, Patel HM, Locke KG, Hood DC, Birch DG. A comparison of visual field sensitivity to photoreceptor thickness in retinitis pigmentosa. *Invest Ophthalmol Vis Sci*. 2010;51:4213–4219.
6. Hood DC, Ramachandran R, Holopigian K, Lazow M, Birch DG, Greenstein VC. Method for deriving visual field boundaries from OCT scans of patients with retinitis pigmentosa. *Biomed Opt Exp*. 2011;2:1106–1114.
7. Moon CH, Park TK, Ohn YH. Association between multifocal electroretinograms, optical coherence tomography and central visual sensitivity in advanced retinitis pigmentosa. *Doc Ophthalmol*. 2012;125:113–122.
8. Panorgias A, Zawadzki RJ, Capps AG, Hunter AA, Morse LS, Werner JS. Multimodal assessment of microscopic morphology and retinal function in patients with geographic atrophy. *Invest Ophthalmol Vis Sci*. 2013;54:4372–4384.
9. Ramachandran R, Zhou L, Locke KG, Birch DG, Hood DCA. Comparison of methods for tracking progression in X-linked retinitis pigmentosa using frequency domain OCT. *Transl Vis Sci Technol*. 2013;2:5.
10. Cai CX, Locke KG, Ramachandran R, Birch DG, Hood DC. A comparison of progressive loss of the ellipsoid zone (EZ) band in autosomal dominant and x-linked retinitis pigmentosa. *Invest Ophthalmol Vis Sci*. 2014;55:7417–7422.
11. Battu R, Khanna A, Hegde B, Berendschot TT, Grover S, Schouten JS. Correlation of structure and function of the macula in patients with retinitis pigmentosa. *Eye*. 2015;29:895–901.
12. Birch DG, Locke KG, Felius J, et al. Rates of decline in regions of the visual field defined by frequency-domain optical coherence tomography in patients with RPGR-mediated X-linked retinitis pigmentosa. *Ophthalmology*. 2015;122:833–839.
13. Talamini CL, Raza AS, Dale EA, Greenstein VC, Odel JG, Hood DC. Abnormal multifocal ERG findings in patients with normal-appearing retinal anatomy. *Doc Ophthalmol*. 2011;123:187–192.
14. Dubra A, Sulai Y, Norris JL, et al. Noninvasive imaging of the human rod photoreceptor mosaic using a confocal adaptive optics scanning ophthalmoscope. *Biomed Opt Exp*. 2011;2:1864–1876.
15. Rossi EA, Chung M, Dubra A, Hunter JJ, Merigan WH, Williams DR. Imaging retinal mosaics in the living eye. *Eye*. 2011;25:301–308.
16. Carroll J, Kay DB, Scoles D, Dubra A, Lombardo M. Adaptive optics retinal imaging-clinical opportunities and challenges. *Curr Eye Res*. 2013;38:709–721.
17. Carroll J, Neitz M, Hofer H, Neitz J, Williams DR. Functional photoreceptor loss revealed with adaptive optics: an alternate cause of color blindness. *Proc Natl Acad Sci U S A*. 2004;101:8461–8466.
18. Genead MA, Fishman GA, Rha J, et al. Photoreceptor structure and function in patients with congenital achromatopsia. *Invest Ophthalmol Vis Sci*. 2011;52:7298–7308.
19. Stepien KE, Martinez WM, Dubis AM, Cooper RF, Dubra A, Carroll J. Subclinical photoreceptor disruption in response to severe head trauma. *Arch Ophthalmol*. 2012;130:400–402.
20. Hansen SO, Cooper RF, Dubra A, Carroll J, Weinberg DV. Selective cone photoreceptor injury in acute macular neuroretinopathy. *Retina*. 2013;33:1650–1658.
21. Ratnam K, Carroll J, Porco TC, Duncan JL, Roorda A. Relationship between foveal cone structure and clinical measures of visual function in patients with inherited retinal degenerations. *Invest Ophthalmol Vis Sci*. 2013;54:5836–5847.
22. Flatter JA, Cooper RF, Dubow MJ, et al. Outer retinal structure after closed-globe blunt ocular trauma. *Retina*. 2014;34:2133–2146.
23. Choi SS, Doble N, Hardy JL, et al. In vivo imaging of the photoreceptor mosaic in retinal dystrophies and correlations with visual function. *Invest Ophthalmol Vis Sci*. 2006;47:2080–2092.

24. Tojo N, Nakamura T, Fuchizawa C, Oiwake T, Hayashi A. Adaptive optics fundus images of cone photoreceptors in the macula of patients with retinitis pigmentosa. *Clin Ophthalmol*. 2013;7:203–210.
25. Duncan JL, Zhang Y, Gandhi J, et al. High-resolution imaging with adaptive optics in patients with inherited retinal degeneration. *Invest Ophthalmol Vis Sci*. 2007;48:3283–3291.
26. Talcott KE, Ratnam K, Sundquist S, et al. Longitudinal study of cone photoreceptors during retinal degeneration and in response to ciliary neurotrophic factor treatment. *Invest Ophthalmol Vis Sci*. 2011;52:2219–2226.
27. Makiyama Y, Ooto S, Hangai M, et al. Macular cone abnormalities in retinitis pigmentosa with preserved central vision using adaptive optics scanning laser ophthalmoscopy. *PLoS One*. 2013;8:e79447.
28. Ratnam K, Västinsalo H, Roorda A, Sankila E-MK, Duncan JL. Cone structure in patients with Usher syndrome type III and mutations in the *Clarin 1* gene. *JAMA Ophthalmol*. 2013;131:67–74.
29. Park SP, Lee W, Bae EJ, et al. Early structural anomalies observed by high-resolution imaging in two related cases of autosomal-dominant retinitis pigmentosa. *Ophthal Surg Lasers Imaging Retina*. 2014;45:469–473.
30. Menghini M, Lujan BJ, Zayit-Soudry S, et al. Correlation of outer nuclear layer thickness with cone density values in patients with retinitis pigmentosa and healthy subjects. *Invest Ophthalmol Vis Sci*. 2015;56:372–381.
31. Zayit-Soudry S, Sippl-Swezey N, Porco T, et al. Repeatability of cone spacing measures in eye with inherited retinal degenerations. *Invest Ophthalmol Vis Sci*. 2015;56:6179–6189.
32. Scoles D, Sulai YN, Langlo CS, et al. In vivo imaging of human cone photoreceptor inner segments. *Invest Ophthalmol Vis Sci*. 2014;55:4244–4251.
33. Horton JC, Parker AB, Botelho JV, Duncan JL. Spontaneous regeneration of human photoreceptor outer segments. *Sci Rep*. 2015;5:12364.
34. Szamier RB, Berson EL. Retinal ultrastructure in advanced retinitis pigmentosa. *Invest Ophthalmol Vis Sci*. 1977;16:947–962.
35. Bunt-Milam AH, Kalina RE, Pagon RA. Clinical-ultrastructural study of a retinal dystrophy. *Invest Ophthalmol Vis Sci*. 1983;24:458–469.
36. Rodrigues MM, Wiggert B, Hackett J, Lee L, Fletcher RT, Chader GJ. Dominantly inherited retinitis pigmentosa: ultrastructure and biochemical analysis. *Ophthalmology*. 1985;92:1165–1172.
37. Flannery JG, Farber DB, Bird AC, Bok D. Degenerative changes in a retina affected with autosomal dominant retinitis pigmentosa. *Invest Ophthalmol Vis Sci*. 1989;30:191–211.
38. Birch DG, Sandberg MA, Berson EL. The Stiles-Crawford effect in retinitis pigmentosa. *Invest Ophthalmol Vis Sci*. 1982;22:157–164.
39. Godara P, Rha J, Tait DM, et al. Unusual adaptive optics findings in a patient with bilateral maculopathy. *Arch Ophthalmol*. 2010;128:253–254.
40. Dubis AM, Cooper RF, Aboshiha J, et al. Genotype-dependent variability in residual cone structure in achromatopsia: Towards developing metrics for assessing cone health. *Invest Ophthalmol Vis Sci*. 2014;55:7303–7311.
41. Song H, Rossi EA, Latchney L, et al. Cone and rod loss in Stargardt Disease revealed by adaptive optics scanning light ophthalmoscopy. *JAMA Ophthalmol*. 2015;133:1198–1203.
42. Pallikaris A, Williams DR, Hofer H. The reflectance of single cones in the living human eye. *Invest Ophthalmol Vis Sci*. 2003;44:4580–4592.
43. Rha J, Jonnal RS, Thorn KE, Qu J, Zhang Y, Miller DT. Adaptive optics flood-illumination camera for high speed retinal imaging. *Opt Express*. 2006;14:4552–4569.
44. Jonnal RS, Besecker JR, Derby JC, et al. Imaging outer segment renewal in living human cone photoreceptors. *Opt Express*. 2010;18:5257–5270.
45. Pircher M, Kroisamer JS, Felberer F, Sattmann H, Götzinger E, Hitzenberger CK. Temporal changes of human cone photoreceptors observed in vivo with SLO/OCT. *Biomed Opt Exp*. 2010;2:100–112.
46. Cooper RF, Dubis AM, Pavaskar A, Rha J, Dubra A, Carroll J. Spatial and temporal variation of rod photoreceptor reflectance in the human retina. *Biomed Opt Exp*. 2011;2:2577–2589.
47. Bruce KS, Harmening WM, Langston BR, Tuten WS, Roorda A, Sincich LC. Normal perceptual sensitivity arising from weakly reflective cone photoreceptors. *Invest Ophthalmol Vis Sci*. 2015;56:4431–4438.
48. Michalakis S, Koch S, Sothilingam V, et al. Gene therapy restores vision and delays degeneration in the CNGB1(-/-) mouse model of retinitis pigmentosa. *Adv Exp Med Biol*. 2014;801:733–739.
49. Tanna H, Dubis AM, Ayub N, et al. Retinal imaging using commercial broadband optical coherence tomography. *Br J Ophthalmol*. 2010;94:372–376.
50. Scoles D, Flatter JA, Cooper RF, et al. Assessing photoreceptor structure associated with ellipsoid zone disruptions visualized with optical coherence tomography. *Retina*. 2016;36:91–103.
51. Huang Y, Cideciyan AV, Papastergiou GI, et al. Relation of optical coherence tomography to microanatomy in normal and *rd* chickens. *Invest Ophthalmol Vis Sci*. 1998;39:2405–2416.
52. Godara P, Cooper RF, Sergouniotis PI, et al. Assessing retinal structure in complete congenital stationary night blindness and Oguchi disease. *Am J Ophthalmol*. 2012;154:987–1001.
53. Wilk MA, McAllister JT, Cooper RF, et al. Relationship between foveal cone specialization and pit morphology in albinism. *Invest Ophthalmol Vis Sci*. 2014;55:4186–4198.
54. Curcio CA, Sloan KR, Kalina RE, Hendrickson AE. Human photoreceptor topography. *J Comp Neurol*. 1990;292:497–523.
55. Dubra A, Harvey Z. Registration of 2D images from fast scanning ophthalmic instruments. In: Fischer B, Dawant B, Lorenz C, eds. *Biomedical Image Registration*. Berlin: Springer-Verlag; 2010;60–71.
56. Packer O, Williams DR. Light, the Retinal Image, and Photoreceptors. In: Shevell SK, ed. *The Science of Color*. New York, NY: OSA & Elsevier Science; 2003:41–102.
57. Garrioch R, Langlo C, Dubis AM, Cooper RF, Dubra A, Carroll J. Repeatability of in vivo parafoveal cone density and spacing measurements. *Optom Vis Sci*. 2012;89:632–643.
58. Schneider CA, Rasband WS, Eliceiri KW. NIH Image to ImageJ: 25 years of image analysis. *Nat Methods*. 2012;9:671–675
59. Liquori A, Vache C, Baux D, et al. Whole USH2A gene sequencing identifies several new deep intronic mutations. *Hum Mutat*. 2016;37:184–193.
60. McGee TL, Seyedahmadi BJ, Sweeney MO, Dryja TP, Berson EL. Novel mutations in the long isoform of the USH2A gene in patients with Usher syndrome type II or non-syndromic retinitis pigmentosa. *J Med Genet*. 2010;47:499–506.
61. Makous W, Carroll J, Wolfing JI, Lin J, Christie N, Williams DR. Retinal microscotomas revealed with adaptive-optics microflashes. *Invest Ophthalmol Vis Sci*. 2006;47:4160–4167.
62. Wang Q, Tuten WS, Lujan BJ, et al. Adaptive optics microperimetry and OCT images show preserved function and recovery of cone visibility in macular telangiectasia type 2 retinal lesions. *Invest Ophthalmol Vis Sci*. 2015;56:778–786.

Investigative Ophthalmology & Visual Science

63. Birch DG, Locke KG, Wen Y, Locke KI, Hoffman DR, Hood DC. Spectral-domain optical coherence tomography measures of outer segment layer progression in patients with X-linked retinitis pigmentosa. *JAMA Ophthalmol*. 2013;131:1143–1150.
64. Ho A, Smith T, Hariri A, et al. Area measurement of the ellipsoid zone (EZ) by SD-OCT and its correlation with visual field identifies a potential anatomical endpoint for clinical trials in retinitis pigmentosa (RP). *Invest Ophthalmol Vis Sci*. 2014;55:3380.
65. Jacob J, Paques M, Krivosic V, et al. Meaning of visualizing retinal cone mosaic on adaptive optics images. *Am J Ophthalmol*. 2015;159:118–123.
66. Enoch JM, Lakshminarayanan V. Retinal fibre optics. In: Cronly-Dillon J, ed. *Vision and Visual Dysfunction*. Boca Raton, FL: CRC Press; 1991:280–309.
67. Stacey A, Pask C. Spatial-frequency response of a photoreceptor and its wavelength dependence. I. Coherent sources. *J Opt Soc Am A Opt Image Sci Vis*. 1994;11:1193–1198.
68. Li KY, Roorda A. Automated identification of cone photoreceptors in adaptive optics retinal images. *J Opt Soc Am A Opt Image Sci Vis*. 2007;24:1358–1363.
69. Chiu SJ, Lokhnygina Y, Dubis AM, et al. Automatic cone photoreceptor segmentation using graph theory and dynamic programming. *Biomed Opt Exp*. 2013;4:924–937.
70. Sharon D, Bruns GA, McGee TL, Sandberg MA, Berson EL, Dryja TP. X-linked retinitis pigmentosa: mutation spectrum of the RPGR and RP2 genes and correlation with visual function. *Invest Ophthalmol Vis Sci*. 2000;41:2712–2721.
71. Audo I, Sahel JA, Mohand-Said S, et al. EYS is a major gene for rod-cone dystrophies in France. *Hum Mutat*. 2010;31:E1406–1435.
72. Bonilha VL, Rayborn ME, Bell BA, et al. Retinal histopathology in eyes from patients with autosomal dominant retinitis pigmentosa caused by rhodopsin mutations. *Graefes Arch Clin Exp Ophthalmol*. 2015;253:2161–2169.
73. Bowne SJ, Daiger SP, Hims MM, et al. Mutations in the RP1 gene causing autosomal dominant retinitis pigmentosa. *Hum Mol Genet*. 1999;8:2121–2128.
74. Dryja TP, McGee TL, Hahn LB, et al. Mutations within the rhodopsin gene in patients with autosomal dominant retinitis pigmentosa. *N Engl J Med*. 1990;323:1302–1307.
75. Dryja TP, McGee TL, Reichel E, et al. A point mutation of the rhodopsin gene in one form of retinitis pigmentosa. *Nature*. 1990;343:364–366.
76. Landrum MJ, Lee JM, Benson M, et al. ClinVar: Public archive of interpretations of clinically relevant variants. *Nucleic Acids Res*. 2016;44:D862–D868.
77. Schorderet DF, Escher P. NR2E3 mutations in enhanced S-cone sensitivity syndrome (ESCS), Goldmann-Favre syndrome (GFS), clumped pigmentary retinal degeneration (CPRD), and retinitis pigmentosa (RP). *Hum Mutat*. 2009;30:1475–1485.
78. Liu XZ, Hope C, Walsh J, et al. Mutations in the myosin VIIA gene cause a wide phenotypic spectrum, including atypical Usher syndrome. *Am J Hum Genet*. 1998;63:909–912.
79. Liu XZ, Walsh J, Mburu P, et al. Mutations in the myosin VIIA gene cause non-syndromic recessive deafness. *Nat Genet*. 1997;16:188–190.
80. Baux D, Larrieu L, Blanchet C, et al. Molecular and in silico analyses of the full-length isoform of usherin identify new pathogenic alleles in Usher type II patients. *Hum Mutat*. 2007;28:781–789.
81. Dreyer B, Brox V, Tranebjaerg L, et al. Spectrum of USH2A mutations in Scandinavian patients with Usher syndrome type II. *Hum Mutat*. 2008;29:451.
82. Le Quesne Stabej P, Saihan Z, Rangesh N. et al. Comprehensive sequence analysis of nine Usher syndrome genes in the UK National Collaborative Usher Study. *J Med Genet*. 2012;49:27–36.
83. Eudy JD, Weston MD, Yao S, et al. Mutation of a gene encoding a protein with extracellular matrix motifs in Usher syndrome type IIa. *Science*. 1998;280:1753–1757.

Investigative Ophthalmology & Visual Science